Symmetry-Constrained Anomalous Transport in the Altermagnetic Material CuX_2 (X = F, Cl)

Zhengxuan Wang[1], Ruqian Wu[2*], Chunlan Ma[3*], Shijing Gong[4], Chuanxi Zhao[5], Shuaikang Zhang[1], Guangtao Wang[1], Tianxing Wang[1], and Yipeng An[1*]

[1]*School of Physics, Henan Normal University, Xinxiang 453007, China*
[2]*Department of Physics and Astronomy, University of California, Irvine 92697, USA*
[3]*School of Physics and Technology, Suzhou University of Science and Technology, Suzhou 215009, China*
[4]*Department of Physics, East China Normal University, Shanghai 200062, China*
[5]*Guangdong Provincial Key Laboratory of Nanophotonic Manipulation, Department of Physics, Jinan University, Guangzhou 511443, China*

(Received 5 April 2025; accepted manuscript online 19 June 2025)

Altermagnetism, a recently identified class of collinear magnetism, combines key features of antiferromagnets and ferromagnets. Despite having zero net magnetization, altermagnetic materials exhibit anomalous transport effects, including the anomalous Hall, Nernst, and thermal Hall effects, as well as magneto-optical Kerr and Faraday effects. These phenomena, previously thought unique to ferromagnets, are dictated by symmetry, as confirmed by density functional theory (DFT) calculations. However, an effective model-based approach to verify these symmetry constraints remains unavailable. In this Letter, we construct a $\boldsymbol{k}\cdot\boldsymbol{p}$ model for d-wave altermagnets CuX_2 (X = F, Cl) using spin space group representations and apply it to calculate the anomalous Hall effect. The symmetry-imposed transport properties predicted by the model are in agreement with the DFT results, providing a foundation for further investigation into symmetry-restricted transport phenomena in altermagnetic materials.

DOI: 10.1088/0256-307X/42/8/080705 CSTR: 32039.14.0256-307X.42.8.080705

Recently, altermagnets have attracted widespread attention as a novel class of collinear magnets. Like conventional collinear antiferromagnets, altermagnets exhibit zero net magnetization.[1] However, they display characteristics akin to ferromagnetic (FM) materials in terms of charge and thermal transport, including the anomalous Hall effect (AHE), anomalous Nernst effect (ANE), and anomalous thermal Hall effect (ATHE).[2] Additionally, while systems with zero net magnetization are typically thought to be incapable of exhibiting the magneto-optical Kerr effect (MOKE) and magneto-optical Faraday effect (MOFE), altermagnets demonstrate non-zero optical Hall conductivity and finite magneto-optical Kerr and Faraday rotation angles.[3]

In traditional collinear antiferromagnetic (AFM) systems, the combination of time-reversal and inversion symmetry ($\mathcal{PT}$ symmetry) guarantees spin degeneracy, as represented by $\mathcal{PT}\varphi_{k\uparrow} = \varphi_{k\downarrow}$. This symmetry spans throughout the entire Brillouin zone, preventing spin splitting. In altermagnetic systems, $\mathcal{PT}$ symmetry is replaced with a combination of rotational and time-reversal symmetry ($\mathcal{RT}$ symmetry). However, the k-invariant subspace of $\mathcal{RT}$ symmetry is limited to only part of the Brillouin zone, allowing spin splitting in regions where $\mathcal{RT}$ symmetry is broken. Such symmetry-enabled spin splitting has already been observed experimentally; for instance, in CrSb (100) thin films, where the spin splitting was directly detected.[4]

Another significant consequence of breaking $\mathcal{PT}$ symmetry is the potential emergence of the AHE. While AHE typically requires breaking time-reversal symmetry and hence is often associated with FM materials, it can also emerge in systems with zero net magnetization when nonmagnetic atoms disrupt time-reversal symmetry. This has been observed in materials like RuO_2, where the effect was initially termed as the crystal Hall effect.[2,5,6] Further studies on RuO_2 led to the introduction of the concept of altermagnetism, a new class of collinear magnets. Notably, although experimental identification of RuO_2 as an altermagnet has remained controversial, a recent study reported spin-splitting magnetoresistance in epitaxial RuO_2 thin films thereby providing conclusive evidence for its altermagnetic character.[7] Altermagnets inherently break time-reversal symmetry making occurrence of AHE without net magnetization possible. In addition, due to the presence of $\mathcal{RT}$ and $\mathcal{P}$ symmetry operations, the components of the anomalous Hall conductivity (AHC) in different directions are subject to symmetry constraints. For instance, in RuO_2 under $M_{001}\mathcal{T}$ symmetry, the AHC component σ_{xy} is constrained to be zero.

ANE[8] and ATHE[9] are thermoelectric analogs of the AHE, exhibiting similar symmetry dependence.[10–17] Like AHE, both ANE and ATHE arise from the breaking of time-reversal symmetry and are closely related to the system's spin–orbit coupling. Systems that exhibit AHE typ-

*Corresponding authors. Email: wur@uci.edu; wlxmcl@mail.usts.edu.cn; ypan@htu.edu.cn
© 2025 Chinese Physical Society and IOP Publishing Ltd. All rights, including for text and data mining, AI training, and similar technologies, are reserved.

ically also show ANE and ATHE, making these properties key characteristics of altermagnets. In particular, the ANE and ATHE, like AHE, are closely linked to the system's symmetry and demonstrate significant temperature dependence, further distinguishing altermagnetic materials from traditional AFM systems.[2] Additionally, altermagnets exhibit non-zero off-diagonal optical conductivity along with MOKE and MOFE. These magneto-optical effects provide additional signatures that set altermagnets apart from AFM materials.[3,18]

Due to the distinct symmetry constraints of altermagnets compared to ferromagnets and antiferromagnets, most previous studies on altermagnetism have not proposed an appropriate model to describe the symmetry-constrainted transport properties of altermagnets. In this Letter, we construct a suitable $\boldsymbol{k}\cdot\boldsymbol{p}$ model based on the recently introduced spin group representation,[19] providing a simple yet direct explanation of the mechanism by which symmetry constraints influence altermagnetic transport properties. The remainder of this Letter is structured as follows. Firstly, we perform the first-principles calculations to obtain band structures of CuX_2, and examine the spin splitting of its valence band on the k_xk_y and k_zk_y planes, which are not protected by $\mathcal{RT}$ symmetry. Subsequently, we constructed a $\boldsymbol{k}\cdot\boldsymbol{p}$ model based on the group representation of their spin space group to verify the symmetry-constrained phenomena of the AHE. Finally, we calculated their anomalous electrical and photoelectrical transport properties. In the main text, we take CuF_2 as a representative example, while results of $CuCl_2$ are provided in the Supplementary Materials (SM).

2. Methods. The electronic structure calculations were performed using the projector augmented wave method as implemented in the Vienna *ab initio* simulation package.[20,21] The exchange-correlation functional was treated within the generalized-gradient approximation with the Perdew–Burke–Ernzerhof parametrization.[22] The lattice parameters were fixed, and the atomic positions were fully relaxed untill the force on each atom was less than 0.001 eV/Å. The energy cutoff was set to 500 eV, with a convergence criterion of 10^{-7} eV. A $15\times11\times11$ k-point grid was used for the Brillouin zone sampling. Following the self-consistent field calculations, maximally localized Wannier functions were constructed by projecting wavefunctions onto s, p, and d orbitals of Cu atoms as well as onto p orbitals of F and Cl atoms, using a uniform $17\times13\times13$ k-point mesh and the WANNIER90 package.[23] Additionally, we utilized the `kdotp-generator` Python package to generate the $\boldsymbol{k}\cdot\boldsymbol{p}$ model.

CuF_2 has a monoclinic structure with lattice constants $a=3.33$ Å, $b=4.61$ Å, and $c=5.41$ Å. The interaxial angles $\alpha=\gamma=90^\circ$ and $\beta=120^\circ$, as illustrated in Fig. 1(a). The crystal structure of CuF_2 belongs to the $P2_1/c$ (No.14) space group, which is generated by two symmetry operations $\{\mathcal{C}_{2y}|(0,1/2,1/2)\}$ and the inversion operation, $\mathcal{P}$. Upon reversing the magnetic moments of the two Cu atoms the unit cell, the system's symmetry group transforms to $\{\mathcal{C}_{2y}\mathcal{T}|(0,1/2,1/2)\}$ and $\mathcal{P}$ symmetry, where $\mathcal{T}$ represents the time-reversal operation. Based on the space group tables,[24] we can readily determine its k-invariant subspace S as illustrated in Fig. 1(b). For k points in S, the relation $\{\mathcal{C}_{2y}\mathcal{T}|(0,1/2,1/2)\}\varphi_{n\boldsymbol{k}\uparrow}=\varphi_{n\boldsymbol{k}\downarrow}$ holds, ensuring the degeneracy of spin-up and spin-down states, as shown in Fig. 1(c). In contrast, for k points outside S, the spin-up and spin-down states $\varphi_{n\boldsymbol{k}\uparrow}$ and $\varphi_{n\boldsymbol{k}\downarrow}$ are not protected by the $\{\mathcal{C}_{2y}\mathcal{T}|(0,1/2,1/2)\}$ operation and can undergo spin splitting as depicted in Fig. 1(d). In the k_xk_y and k_zk_y planes, CuF_2 can be identified as a prototypical d-wave altermagnet with spin-momentum locking as shown in Figs. 1(e) and 1(f).

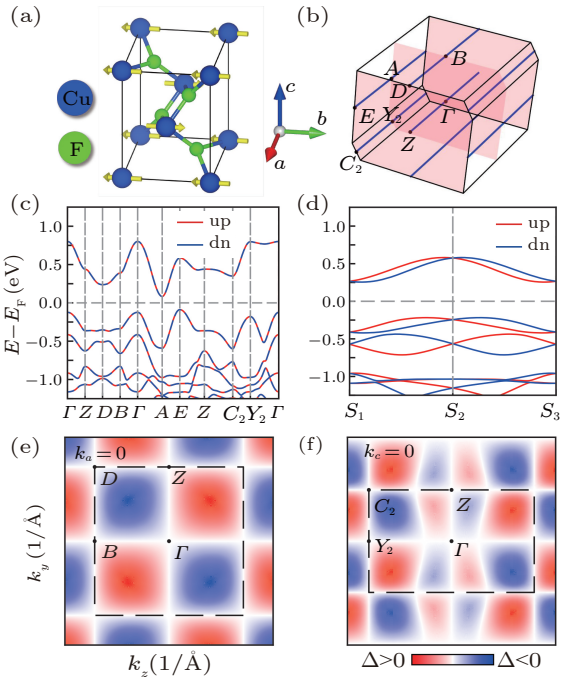

Fig. 1. (a) and (b) The crystal structure and the Brillouin zone of CuF_2 respectively. The red face and blue line represent the k-invariant subspace of symmetry $\{\mathcal{C}_{2y}\mathcal{T}|(0,1/2,1/2)\}$. (c) and (d) The band structure along the path which $\boldsymbol{k}$ belong and does not belong to the invariant subspace of the symmetry operation $\{\mathcal{C}_{2y}\mathcal{T}|(0,1/2,1/2)\}$, respectively. $S_1=(0,-1/2,1/2)$, $S_2=(0,0,1/2)$ and $S_3=(0,1/2,1/2)$. (e) and (f) The spin splitting in the k_zk_y plane and k_xk_y plane, respectively. The dash lines indicate the boundaries of the first Brillouin zone, and the colors correspond to $\Delta=\varepsilon_\uparrow-\varepsilon_\downarrow$.

3. The $\boldsymbol{k}\cdot\boldsymbol{p}$ Model Hamiltonian. Due to the breaking of $\mathcal{PT}$ symmetry, the altermagnet cannot be fully described by its space group or magnetic space group. For instance, CuF_2 belongs to 14.79 (BNS number) magnetic space group, but the irreducible representation of this magnetic space group at the Γ point is one-dimensional, contradicting to that obtained from DFT calculations. Therefore, to describe altermagnets, a spin space group with additional symmetry operations is required for capturing the symmetry constraints and constructing an appropriate model. The CuF_2 system belongs to spin group 14.1.2.3.L

Table 1. The symmetry operations of the CuF_2 material in the spin space group 14.1.2.3.L, along with their spin group representations. The rotation operation matrices are written in the lattice coordinate system, while the spin rotation operations are written in the Cartesian coordinate system.

	Operation 1			Operation 2			Operation 3			Operation 4		
	Rotation	Spin rotation	Tau	Rotation	Spin rotation	Tau	Rotation	Spin rotation	Tau	Rotation	Spin rotation	Tau
	$\begin{pmatrix}1&0&0\\0&1&0\\0&0&1\end{pmatrix}$	$\begin{pmatrix}1&0&0\\0&1&0\\0&0&1\end{pmatrix}$	$\begin{pmatrix}0\\0\\0\end{pmatrix}$	$\begin{pmatrix}-1&0&0\\0&-1&0\\0&0&-1\end{pmatrix}$	$\begin{pmatrix}1&0&0\\0&1&0\\0&0&1\end{pmatrix}$	$\begin{pmatrix}0\\0\\0\end{pmatrix}$	$\begin{pmatrix}-1&0&0\\0&1&0\\0&0&-1\end{pmatrix}$	$\begin{pmatrix}-1&0&0\\0&-1&0\\0&0&-1\end{pmatrix}$	$\begin{pmatrix}0\\\frac{1}{2}\\\frac{1}{2}\end{pmatrix}$	$\begin{pmatrix}1&0&0\\0&-1&0\\0&0&1\end{pmatrix}$	$\begin{pmatrix}-1&0&0\\0&-1&0\\0&0&-1\end{pmatrix}$	$\begin{pmatrix}0\\\frac{1}{2}\\\frac{1}{2}\end{pmatrix}$
Γ_1		$\begin{pmatrix}1&0\\0&1\end{pmatrix}$			$\begin{pmatrix}1&0\\0&1\end{pmatrix}$			$\begin{pmatrix}0&\mathrm{i}\\-\mathrm{i}&0\end{pmatrix}$			$\begin{pmatrix}0&\mathrm{i}\\-\mathrm{i}&0\end{pmatrix}$	
Γ_2		$\begin{pmatrix}1&0\\0&1\end{pmatrix}$			$\begin{pmatrix}-1&0\\0&-1\end{pmatrix}$			$\begin{pmatrix}0&\mathrm{i}\\-\mathrm{i}&0\end{pmatrix}$			$\begin{pmatrix}0&-\mathrm{i}\\\mathrm{i}&0\end{pmatrix}$	

which includes four symmetry operations. At the Γ point, it has two two-dimensional irreducible representations that link the spin-up and spin-down states, as shown in Table 1.

To obtain all the symmetries of 14.1.2.3.L, we construct the $\boldsymbol{k}\cdot\boldsymbol{p}$ model based on the two degenerate spin-up and spin-down states at the valence band maximum at the Γ point, represented by Γ_1. The resulting $\boldsymbol{k}\cdot\boldsymbol{p}$ Hamiltonian is given by

$$\begin{aligned} H(\boldsymbol{k}) = {} & (c_0 + c_4k_y + c_8k_x^2 + c_{12}k_xk_z + c_{13}k_y^2 + c_{17}k_z^2)\sigma_0 \\ & + (c_1k_x + c_5k_z + c_9k_xk_y + c_{14}k_yk_z)\sigma_1 \\ & + (c_2k_x + c_6k_z + c_{10}k_xk_y + c_{15}k_yk_z)\sigma_2 \\ & + (c_3k_x + c_7k_z + c_{11}k_xk_y + c_{16}k_yk_z)\sigma_3\,, \end{aligned} \tag{1}$$

where $\sigma_0, \sigma_1, \sigma_2$, and σ_3 are the Pauli matrices. We fit this Hamiltonian along the diagonal direction of the Brillouin zone using the DFT-derived energy bands, and the fitting result is shown in the small inset of Fig. 2(a). For a two-band model, the Hamiltonian can always be decompose into the following form:

$$H(\boldsymbol{k}) = \varepsilon_0(\boldsymbol{k}) + \boldsymbol{h}(\boldsymbol{k})\cdot\boldsymbol{\sigma}\,, \tag{2}$$

where $\boldsymbol{h}(\boldsymbol{k})$ is the non-diagonal term of the Hamiltonian decomposed into a vector form with the Pauli matrices. From this, we can obtain the Berry curvature in a simple way,

$$\Omega_z(\boldsymbol{k}) = -\frac{1}{2h^3}\boldsymbol{h}(\boldsymbol{k})\cdot\frac{\partial\boldsymbol{h}(\boldsymbol{k})}{\partial k_x}\times\frac{\partial\boldsymbol{h}(\boldsymbol{k})}{\partial k_y}\,. \tag{3}$$

The calculated Ω_x, Ω_y, and Ω_z on the $k_y = 0$ plane are shown in Figs. 2(b)–2(d). It is clear that under the $M_{010}\mathcal{T}$ symmetry operation, Ω_y is an odd function, and its integral over the Brillouin zone is always zero. This intriguing distribution of the Berry curvature arises from the $M_{010}\mathcal{T}$ symmetry operation inherent in CuF_2, which enforces Ω_y to be an odd function along the k_y direction. This property can be directly derived from both the Berry curvature's Kubo formula and the aforementioned equations. As a consequence, the AHC component σ_{zx} vanishes.

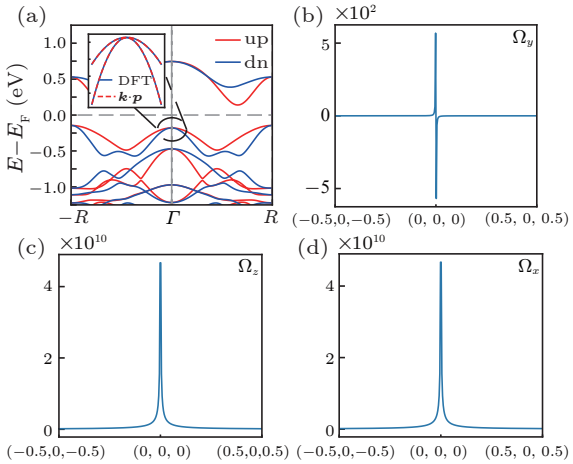

Fig. 2. (a) The band structure along the diagonal direction of the Brillouin zone passing through the Γ point. The inset shows a comparison between the $\boldsymbol{k}\cdot\boldsymbol{p}$ model and DFT calculations near the Γ point. (b), (c), and (d) The Berry curvatures Ω_y, Ω_x, and Ω_z calculated on the $k_y = 0$ plane using the $\boldsymbol{k}\cdot\boldsymbol{p}$ model.

4. Anomalous Transport Properties. Altermagnets exhibit anomalous transport properties that are distinct from those of AFM. These anomalies include non-zero AHC, anomalous Nernst conductivity (ANC), and anomalous thermal Hall conductivity (ATHC) in the absence of net magnetization. The intrinsic origin of these anomalous transport phenomena in altermagnets can be attributed to the non-zero Berry curvature integral due to the energy splitting between up and down spin states in the Brillouin zone. Since these three transport properties share the same underlying physics, we focus on the AHC to discuss how symmetry affects them. The AHC, ANC and ATHC can be expressed as[25–27]

$$\sigma_{xy}^{\mathrm{AHC}} = -\frac{e^2}{\hbar}\int\frac{\mathrm{d}^3\boldsymbol{k}}{(2\pi)^3}\Omega_z(\boldsymbol{k}), \tag{4}$$

$$\alpha_{xy}^{\mathrm{ANC}} = \int\frac{\varepsilon-\mu}{eT}\left(-\frac{\partial f}{\partial\varepsilon}\right)\sigma_{xy}^{\mathrm{AHC}}\mathrm{d}\varepsilon, \tag{5}$$

$$k_{xy}^{\mathrm{ATHC}} = \int\frac{(\varepsilon-\mu)^2}{e^2T}\left(-\frac{\partial f}{\partial\varepsilon}\right)\sigma_{xy}^{\mathrm{AHC}}\mathrm{d}\varepsilon, \tag{6}$$

where $\Omega_z(\boldsymbol{k})$ is the momentum-resolved Berry curvature, μ is the chemical potential, and $f = 1/[\exp((\varepsilon-\mu)/k_{\rm B}T)+1]$ is the Fermi–Dirac distribution function.

The AHC is strongly influenced by mirror symmetries, which cause certain components to vanish under specific symmetry operations. For instance, under the M_{001} symmetry, the σ_{yz} and σ_{zx} components change sign, while σ_{xy} remains invariant. In this case, we have $\sigma_{yz} = \sigma_{zx} = 0$. For a combined time-reversal and mirror symmetry operation, such as $M_{001}\mathcal{T}$, only σ_{xy} is affected, resulting in $\sigma_{xy} = 0$. This behavior of AHC leads to the suppression of specific AHC components in systems with multiple mirror symmetries. For example, in RuO_2, the presence of mirror symmetries depends on the magnetization direction.[2]

In contrast, for the CuF_2 system, the unique mirror symmetry is coupled with the time-reversal operation as $\{M_{010}\mathcal{T}|(0,1/2,1/2)\}$. This symmetry is independent of the magnetization direction. As a result, the σ_{xy} and σ_{yz} components are always non-zero, while σ_{zx} remains zero.

The same symmetry constraints can be applied to the ANC and the ATHC, since they share the same symmetry structure as AHC. Their behaviors with respect to the changes in magnetization direction follow the same manner. The magnetic reorientation can break or restore the mirror symmetries, leading to significant modulation of all three transport properties. Significantly, the periodic modulation of AHC with respect to magnetization direction also manifests in ANC and ATHC.

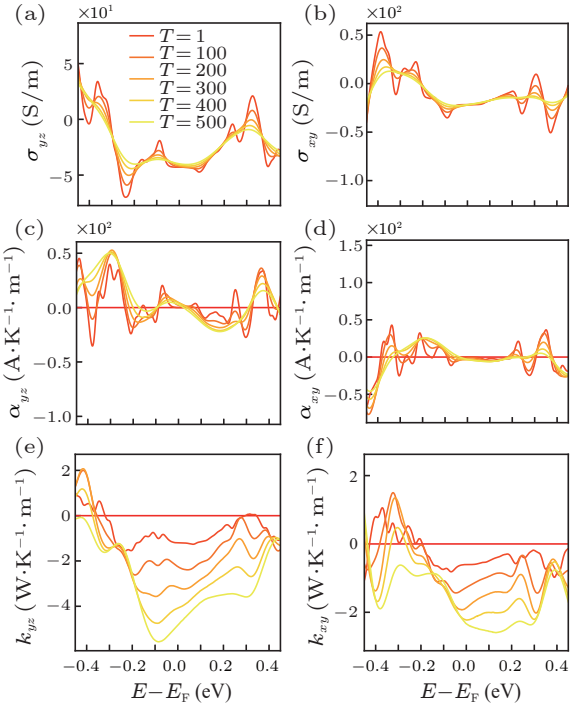

Fig. 3. Temperature-dependent behavior of various transport coefficients. Panels (a) and (b) show the AHC components of σ_{yz} and σ_{xy}, respectively, as a function of the energy. Panels (c) and (d) depict the ANC components of α_{yz} and α_{xy}, respectively, as a function of the energy. Panels (e) and (f) illustrate the ATHC components of k_{yz} and k_{xy}, respectively, as a function of the energy. The curves in all panels represent different temperatures, with each color corresponding to a specific temperature in Kelvin. Due to the sharp peak in anomalous Hall conductivity at $T = 1\,$K, the corresponding data has been placed in the SM.

Based on Eqs. (4)–(6), we calculate the temperature-dependent AHC, ANC, and ATHE. As shown in Figs. 3(a)–3(f). AHC is very small and shows little variation with temperature around the Fermi level. However, through electron or hole doping, AHC can be significantly enhanced. By shifting the Fermi level (between $-0.5\,$eV and $0.5\,$eV), σ_{yz} may reach a peak value of $-70.3\,$S/m at $T = 100\,$K and $E - E_{\rm F} = -0.23\,$eV, while σ_{xy} peaks at $53.2\,$S/m at $E - E_{\rm F} = -0.38\,$eV under the same temperature. For the thermoelectric coefficients, α_{yz} achieves a peak value of $52.4\,\mathrm{A{\cdot}K^{-1}{\cdot}m^{-1}}$ at $T = 300\,$K and $E - E_{\rm F} = -0.29\,$eV, and α_{xy} peaks at $-77.2\,\mathrm{A{\cdot}K^{-1}{\cdot}m^{-1}}$ at $T = 200\,$K and $E - E_{\rm F} = -0.44\,$eV. The ATHC is directly proportional to temperature, with peak values occurring at $T = 500\,$K. Specifically, κ_{yz} reaches a peak of $-5.59\,\mathrm{W{\cdot}K^{-1}{\cdot}m^{-1}}$ at $E-E_{\rm F} = -0.08\,$eV, and κ_{xy} peaks at $-2.64\,\mathrm{W{\cdot}K^{-1}{\cdot}m^{-1}}$ at $E-E_{\rm F} = 0.13\,$eV. Notably, the AHC of CuF_2 is non-zero within the band gap formed between the valence band and the conduction band. This is attributed to the spin splitting of CuF_2 in the Brillouin zone, which is similar to the intrinsic AHC observed in FM materials.

5. The MOKE and MOFE. A special characteristic of altermagets is that they exhibit magneto-optical properties with a net-zero magnetic moment, similar to FM systems. This indicates that they have a non-zero optical Hall conductivity. To calculate MOKE and MOFE, we compute the conductivity using the Kubo–Greenwood formula,[28,29]

$$\sigma_{xy}(\omega) = \frac{\mathrm{i}e^2\hbar}{N_k\Omega_{\rm c}}\sum_{\boldsymbol{k}}\sum_{n,m}\frac{f_{m\boldsymbol{k}}-f_{n\boldsymbol{k}}}{\varepsilon_{m\boldsymbol{k}}-\varepsilon_{n\boldsymbol{k}}} \times \frac{\langle\psi_{n\boldsymbol{k}}|v_\alpha|\psi_{m\boldsymbol{k}}\rangle\langle\psi_{m\boldsymbol{k}}|v_\beta|\psi_{n\boldsymbol{k}}\rangle}{\varepsilon_{m\boldsymbol{k}}-\varepsilon_{n\boldsymbol{k}}-(\hbar\omega+\mathrm{i}\eta)}, \tag{7}$$

where $\Omega_{\rm c}$ is the cell volume, N_k is the total number of k points used for sampling the Brillouin zone, $\psi_{n\boldsymbol{k}}$ and $\varepsilon_{n\boldsymbol{k}}$ are respectively the Wannier function and interpolated energy of band n at momentum $\boldsymbol{k}$, $v_{\alpha,\beta}$ are velocity operators, $f_{n\boldsymbol{k}}$ is the Fermi–Dirac distribution function, $\hbar\omega$ is the photon energy, and η is an adjustable energy smearing parameter.

For the complex Kerr and Faraday angles, we adopt simplified expressions under the assumption of a small rotation angle,[30–38]

$$\phi_{\rm K}^z = \vartheta_{\rm K}^z + \mathrm{i}\varepsilon_{\rm K}^z \approx \frac{-\nu_{xyz}\sigma_{xy}}{\sigma_0\sqrt{1+\mathrm{i}(4\pi/\omega)\sigma_0}}, \tag{8}$$

$$\phi_{\rm F}^z = \vartheta_{\rm F}^z + \mathrm{i}\varepsilon_{\rm F}^z \approx \frac{-\nu_{xyz}\sigma_{xy}}{\sqrt{1+\mathrm{i}(4\pi/\omega)\sigma_0}}\frac{2\pi}{c}, \tag{9}$$

where $\sigma_0 = (\sigma_{xx}+\sigma_{yy})/2$. Detailed calculation steps can be found in the SM.

Based on Eq. (7), when the system exhibits mirror time-reversal ($\{M_{010}\mathcal{T}|(0,1/2,1/2)\}$) symmetry, the off-diagonal components of the optical conductivity tensor are constrained. Specifically, the off-diagonal element σ_{zx}

changes sign under $\{M_{010}\mathcal{T}|(0,1/2,1/2)\}$ symmetry, while σ_{xy} and σ_{yz} remain invariant. As a result σ_{zx} vanishes, as shown in Fig. 4(b). Since both the Kerr and Faraday angles depend on the same off-diagonal terms, their spectra exhibit similar trend; i.e., $\phi_{\mathrm{K}k_y} = 0$ and $\phi_{\mathrm{K}k_y} = 0$, as shown in Figs. 4(c)–4(f). The peak value of the Kerr angle in the z direction can be as large as 0.15 deg at 3.09 eV; while in the x direction, the peak value is also appreciable at -0.07 deg at 3.18 eV. The peak value of the Faraday angle in the z direction is approximately 221 deg/cm at 5.54 eV; while in the x direction, the peak value is around 62 deg/cm at 5.31 eV.

Since $CuCl_2$ shares the same crystal structure as CuF_2, its AHC, ANC, ATHC, and magneto-optical effects exhibit similar behavior to those of CuF_2. The detailed computational results for $CuCl_2$ are provided in the SM.

In summary, altermagnets exhibit transport properties distinct from those of traditional collinear AFM materials, and these transport properties are strictly constrained by symmetry. Note that neither the space group nor the magnetic space group can fully describe these constraints; thus, one must use a spin space group with more comprehensive symmetry operations to construct a model for studies of altermagnets. This work provides a method for studying the symmetry-constrained transport properties of altermagnets and demonstrates successful applications for CuX_2. DFT calculations and $\boldsymbol{k}\cdot\boldsymbol{p}$ model analysis indicate spin splitting in the bounds of CuF_2 in certain reegions of the Brillouin zone. This leads to significant contributions to direct-current transport as well as magneto-optical effects. There findings are very promoting for the design of innovative spintronic devices with exotic transport, magnonic and optical features.

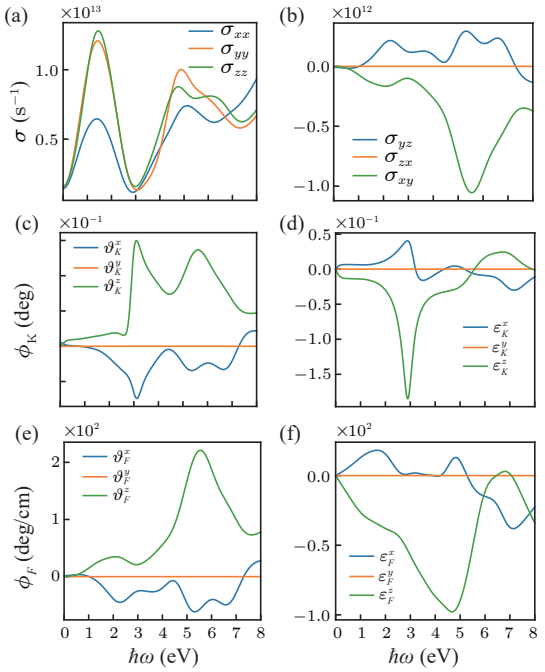

Fig. 4. Magneto-optical and optical conductivity properties. Panel (a) shows the diagonal component of the optical conductivity, while panel (b) presents the off-diagonal component. Panels (c) and (d) display the magneto-optical Kerr angle with (c) showing the rotation angle and (d) showing the ellipticity. Panels (e) and (f) illustrate the magneto-optical Faraday angle, with (e) showing the rotation angle and (f) showing the ellipticity.

The data that support the findings of this study are available from the contact author upon reasonable request.

Acknowledgments. This work was supported by the National Natural Science Foundation of China (Grant No. 12274117), the Natural Science Foundation of Henan (Grant No. 242300421214), the Program for Innovative Research Team (in Science and Technology) in the University of Henan Province (Grant No. 24IRTSTHN025), the Open Fund of Guangdong Provincial Key Laboratory of Nanophotonic Manipulation (No. 202502) and Guangdong S&T Program (No. 2023B1212010008), and the High-Performance Computing Center of Henan Normal University. Work at UCI was supported by the U.S. DOE, Office of Science (Grant No. DE-FG02-05ER46237).

References

[1] Duan X, Zhang J, Zhu Z, Liu Y, Zhang Z, Žutić I, and Zhou T 2025 *Phys. Rev. Lett.* **134** 106801
[2] Zhou X, Feng W, Zhang R W, Šmejkal L, Sinova J, Mokrousov Y, and Yao Y 2024 *Phys. Rev. Lett.* **132** 056701
[3] Zhou X, Feng W, Yang X, Guo G Y, and Yao Y 2021 *Phys. Rev. B* **104** 024401
[4] Liao S, Li X, Chen X, Yu Z, Yao J, Xu R, Sun J, Liu Z, Shen D, Wang Y, Feng D, and Jiang J 2025 *Chin. Phys. Lett.* **42** 067503
[5] Šmejkal L, González-Hernández R, Jungwirth T, and Sinova J 2020 *Sci. Adv.* **6** eaaz8809
[6] Feng Z, Zhou X, Šmejkal L *et al.* 2022 *Nat. Electron.* **5** 735
[7] Chen H, Wang Z A, Qin P, Meng Z, Zhou X, Wang X, Liu L, Zhao G, Duan Z, Zhang T, Liu J, Shao D F, Jiang C, and Liu Z 2025 *Adv. Mater.* 2507764
[8] Xiao D, Yao Y, Fang Z, and Niu Q 2006 *Phys. Rev. Lett.* **97** 026603
[9] Qin T, Niu Q, and Shi J 2011 *Phys. Rev. Lett.* **107** 236601
[10] Onose Y, Shiomi Y, and Tokura Y 2008 *Phys. Rev. Lett.* **100** 016601
[11] Shiomi Y, Onose Y, and Tokura Y 2009 *Phys. Rev. B* **79** 100404
[12] Shiomi Y, Onose Y, and Tokura Y 2010 *Phys. Rev. B* **81** 054414
[13] Smith A W 1911 *Phys. Rev. (Series I)* **33** 295
[14] Smith A W 1921 *Phys. Rev.* **17** 23
[15] Lee W L, Watauchi S, Miller V L, Cava R J, and Ong N P 2004 *Phys. Rev. Lett.* **93** 226601
[16] Miyasato T, Abe N, Fujii T, Asamitsu A, Onoda S, Onose Y, Nagaosa N, and Tokura Y 2007 *Phys. Rev. Lett.* **99** 086602
[17] Onoda S, Sugimoto N, and Nagaosa N 2008 *Phys. Rev. B* **77** 165103
[18] Bai L, Feng W, Liu S, Šmejkal L, Mokrousov Y, and Yao Y *Adv. Funct. Mater.* **34** 2409327
[19] Jiang Y, Song Z, Zhu T, Fang Z, Weng H, Liu Z X, Yang J, and Fang C 2024 *Phys. Rev. X* **14** 031039
[20] Kresse G and Furthmüller J 1996 *Comput. Mater. Sci.* **6** 15
[21] Blöchl P E 1994 *Phys. Rev. B* **50** 17953
[22] Perdew J P, Burke K, and Ernzerhof M 1996 *Phys. Rev. Lett.* **77** 3865

[23] Mostofi A A, Yates J R, Lee Y S, Souza I, Vanderbilt D, and Marzari N 2008 *Comput. Phys. Commun.* **178** 685

[24] Aroyo M I, Kirov A, Capillas C, Perez-Mato J M, and Wondratschek H 2006 *Acta Cryst.* **62** 115

[25] Ehrenreich H and Spaepen F 2001 *Solid State Physics* Vol. 56 (Academic Press)

[26] Behnia K 2015 *Fundamentals of Thermoelectricity* (Oxford University Press)

[27] van Houten H, Molenkamp L W, Beenakker C W J, and Foxon C T 1992 *Semicond. Sci. Technol.* **7** B215

[28] Mostofi A A, Yates J R, Lee Y S, Souza I, Vanderbilt D, and Marzari N 2008 *Comput. Phys. Commun.* **178** 685

[29] Yates J R, Wang X, Vanderbilt D, and Souza I 2007 *Phys. Rev. B* **75** 195121

[30] Feng W, Guo G Y, Zhou J, Yao Y, and Niu Q 2015 *Phys. Rev. B* **92** 144426

[31] Wimmer S, Mankovsky S, Minár J, Yaresko A N, and Ebert H 2019 *Phys. Rev. B* **100** 214429

[32] Zhou X, Hanke J P, Feng W, Li F, Guo G Y, Yao Y, Blügel S, and Mokrousov Y 2019 *Phys. Rev. B* **99** 104428

[33] Guo G Y and Ebert H 1995 *Phys. Rev. B* **51** 12633

[34] Ravindran P, Delin A, James P, Johansson B, Wills J M, Ahuja R, and Eriksson O 1999 *Phys. Rev. B* **59** 15680

[35] Feng W, Guo G Y, and Yao Y 2016 *2D Mater.* **4** 015017

[36] Zhou X, Feng W, Li F, and Yao Y 2017 *Nanoscale* **9** 17405

[37] Li F, Zhou X, Feng W, Fu B, and Yao Y 2018 *New J. Phys.* **20** 043048

[38] Zhou X, Li F, Xing Y, and Feng W 2019 *J. Mater. Chem. C* **7** 3360